

# Morphing Tokens Draw Strong Masked Image Models

Taekyung Kim\*, Byeongho Heo, and Dongyoon Han\*

NAVER AI Lab

**Abstract.** Masked image modeling (MIM) is a promising option for training Vision Transformers among various self-supervised learning (SSL) methods. The essence of MIM lies in token-wise masked token predictions, with targets tokenized from images or generated by pre-trained models such as vision-language models. While tokenizers or pre-trained models are plausible MIM targets, they often offer spatially inconsistent targets even for neighboring tokens, complicating models to learn unified discriminative representations. Our pilot study confirms that addressing spatial inconsistencies has the potential to enhance representation quality. Motivated by the findings, we introduce a novel self-supervision signal called Dynamic Token Morphing (DTM), which dynamically aggregates contextually related tokens to yield contextualized targets. DTM is compatible with various SSL frameworks; we showcase an improved MIM by employing DTM, barely introducing extra training costs. Our experiments on ImageNet-1K and ADE20K demonstrate the superiority of our methods compared with state-of-the-art, complex MIM methods. Furthermore, the comparative evaluation of the iNaturalists and fine-grained visual classification datasets further validates the transferability of our method on various downstream tasks. Code is available at <https://github.com/naver-ai/dtm>.

## 1 Introduction

Since the success of Vision Transformer (ViT), numerous training strategies have arisen for ViT [15], including self-supervised learning (SSL) methods [7, 10, 18, 20]. Recent advances in masked image modeling (MIM) [4, 19, 52] have established it as a mainstream SSL approach for ViT. In essence, the crux of the MIM methods lies in leveraging token-wise optimization objectives derived from predicting masked tokens to given targets. Consequently, MIM methods have explored various approaches to generate effective target tokens, employing various pre-trained models including vision-language models [5, 34], utilizing momentum teachers [4, 56] or directly exploiting patchified images [19, 52].

While tokenizers or pre-trained models have proven their potential as promising MIM targets [5, 27, 34, 49], we argue the pre-trained models tend to generate spatially noisy token representations of class information (*e.g.*, inconsistent

---

\* Equal contribution

class labels), and their utilization as pre-training targets may incur negative impacts (See §3). For example, a pre-trained vision-language model reveals spatially inconsistent prediction results, as shown in Fig. 1. To delve deeper into the behaviors of token representations from pre-trained models, we analyze the impacts of spatially inconsistent representations from the perspective of discriminability and training capability. We initially observe reduced discriminability in zero-shot image classification and linear probing without token aggregation, also revealed with our continuous metric. Furthermore, another pilot distillation experiment reveals that the targets derived from a token aggregation method, not aware of context, disrupts pre-training. Unlikely, the model supervised by aggregated target tokens with context enjoys the potential of enhanced representation. Consequently, spatially inconsistent targets challenge learning one-to-one token maps, leading to suboptimal representation learning.

Bearing those in mind, we introduce a novel token contextualization method Dynamic Token Morphing (DTM), where *token morphing* is a process that links contextually similar tokens and aggregates them for coherent and comprehensive representations. We conjecture that training should be accelerated by the guidance provided by composite representations of morphed tokens, derived from the aggregation of contextually related tokens (see Fig. 3). Specifically, we encode the token-wise target representations and derive matching relations among tokens through DTM. The merging process is performed for both tokens regarding the matching relation and aligning each morphed token with the corresponding morphed target tokens. The range of morphing can vary from a single token to the entire tokens, covering from token-wise to image-level representation learning. While there are many options, we simply opt for bipartite matching for morphing, achieving both efficiency and efficacy.

Through extensive experiments, we verify our method’s general applicability and scalability. DTM improves fine-tuning accuracies as equipped with various SSL frameworks, affirming its general applicability as a basic element. Moreover, DTM consistently enhances the baselines from ViT-S/16 to ViT-L/16 with large margins, demonstrating its scalability. Comparison with previous SSL methods verifying its superiority. Our method showcases further transferability on the iNaturalist and fine-grained visual classification datasets.

## 2 Related Work

**Masked image modeling.** Inspired by the promising performance of masked language modeling (MLM), BEiT [5] successfully extends MLM into the computer vision domain, using an external offline tokenizer from Dall-E [36]. iBOT [56] jointly trains the target encoder and the online tokenizer to remove the dependency on the external tokenizer. Data2vec [4] incorporates a momentum encoder to perform feature-level masked prediction tasks, leveraging representations from the multiple layers of neural networks. MAE [19] and SimMIM [52] demonstrate efficient masked image modeling by directly reconstructing masked input pixels without any tokenizer. On the other hand, several attempts have been made

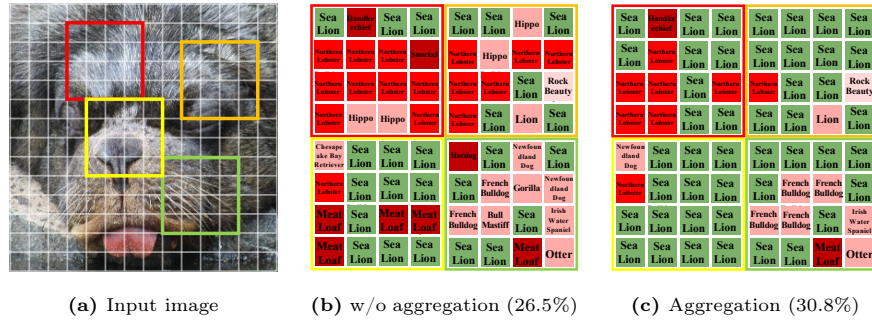


**Fig. 1: What is the spatial inconsistency?** We visualize *token-wise zero-shot classification* results to visualize the spatially inconsistent token predictions. The given input images in (a), two following results (b) and (c) show the predicted classes for each token in the bounding boxes without and with token aggregations (*e.g.*, clustering, or morphing), respectively. Furthermore, we depict the differences between the predicted and ground-truth classes by varying the lightness of **red**, whereas the **green** represents the correct prediction. Each result yields 113 and 82 corrected tokens, respectively; therefore, we say that aggregation gives fewer spatially inconsistent representations.

to exploit the pre-trained model as a tokenizer. BEiT v2 [34] pre-train a codebook for CLIP [35] to discretize a semantic space. MVP [48] exploits a tokenizer pre-trained with multimodal data to enhance the semantics for MIM. A line of studies [38, 49] using CLIP as a teacher to generate target representations have also been highlighted. Our method aims to utilize a teacher model more effectively, including CLIP, rather than just using it as a raw pre-trained model.

**Token aggregation methods.** Token aggregation can conceptually be categorized as a token clustering method and usually aims for efficiency. Hard clustering methods like K-Means [30], K-Medoids [1], and Density-Peak Clustering with K-Nearest Neighbors (DPC-KNN) [23] enforce each data to belong to a single cluster exclusively. Bipartite matching [24] also aggregates data in a hard clustering manner, which optimizes pairs elements from two disjoint sets given objective function. Meanwhile, soft clustering is defined to let data belong to multiple clusters. LIT [33] employs deformable token merging layers to aggregate tokens between stages. Furthermore, some token pruning methods [28, 37, 40, 53] can be categorized into token aggregation methods; however, they intensely focused on compressing tokens to aim for a cost-efficient vision transformer. While the above token aggregation methods have mainly been employed to boost efficiency, our approach diverges significantly. We take the concept of token aggregation to address spatially noisy target tokens in token-level supervision, thereby enhancing the efficacy of MIM in terms of precision.

### 3 Pilot Study

In this section, we study the behavior of token representations generated by pre-trained models and their negative impacts on pre-training.

**Spatial Inconsistency.** We begin by visualizing token representations from a vision-language model [35] to illustrate spatial inconsistency. The inconsistent class predictions observed on each patch, as depicted in Fig. 1, reveal noisy token representations.

**Impact of Spatial Inconsistency.** The spatially noisy token representations has the potential to lead to an underestimation of the capabilities of the vision-language models. To understand the extent of these effects, we quantitatively assess various metrics at a dataset scale in Table 1. The quantitative analyses reveal that enhancing spatial coherence in the token representations results in improved performance, thus highlighting the importance of addressing spatial inconsistency.

**Spatial Inconsistency in Representation Learning.** The lack of spatial coherence in token representations have substantial negative impacts on the representation learning. Utilizing such noisy representations as targets can undermine the capabilities of the models. We employ representation learning to assess token aggregation methods to confirm the efficacy of handling spatial inconsistency via a refined context-aware method.

### 3.1 Spatial Inconsistency

We define the spatial inconsistency among token representations with an illustrative example. Given the input image in Fig. 1a, we visualize the token-wise predictions without and with token aggregation in Fig. 1b and 1c, respectively. Correct and incorrect tokens are marked in green and red, respectively, with a gradient to darker shades of red, indicating a more significant deviation from the true class. Despite the proximity and contextual similarity among tokens, wrong tokens in the green box (bottom right) in Fig. 1b exhibit spatially inconsistent prediction results (French Bulldog, Gorilla, Bull Mastiff, Hotdog, and Newfoundland Dog) while tokens in Fig. 1c show correct or relatively consistent predictions (french bulldog). Moreover, token aggregation for predictions yields improved accuracy, with 113 correct tokens out of 196 and a gap of 31 tokens compared to the counterpart. The comparison between the two prediction results highlights the spatial inconsistency among tokens from a pre-trained model, which could potentially disrupt representation learning when used as targets.

**Table 1: Handling spatial inconsistency boosts accuracy.** We compare the ImageNet-1K accuracy of zero-shot/linear probing via average pooled token-wise logit. Post-hoc morphed patch representations enhance accuracies, indicating that addressing spatial inconsistency improves precision. Linear probing is trained for 25 epochs, and we use the fixed half of the whole tokens for aggregation.

Token Aggregation	Zero-shot image classification (%)	Linear probing (%)	Averaged patch-wise cosine similarity with [CLS]
	26.5	73.2	0.53
✓	30.8 (+4.3)	77.6 (+3.2)	0.56 (+0.3)

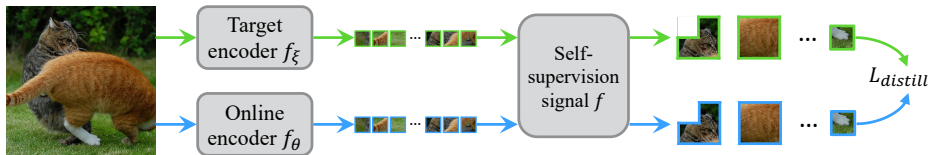


**Fig. 2: Representation learning with various supervisions.** We illustrate our study’s base representation learning framework along with different self-supervision signal function  $f$ . We evaluate four variants of the self-distillation target: (1) token-wise supervision (baseline), (2) downsampled supervision (3) supervision after bipartite matching layer-wise, (4) superpixel supervision, and (5) supervision by token morphing.

### 3.2 Impact of Spatial Inconsistency

To quantitatively assess the impact of spatial inconsistency at a dataset scale, we compute the token-wise ensemble prediction using a global pool, with and without token aggregations. Fundamentally, we predict class scores for each token and average these scores across all tokens within the given image. When predicting with token aggregation, we group semantically relevant tokens and average their representations group-wise prior to token-wise ensemble prediction. We employ CLIP-B/16 [35] for our study, so we aggregate 98 tokens for token aggregation, which occupy half of the entire tokens.

Table 1 reports the results of zero-shot image classification, linear probing, and averaged cosine similarity between the [CLS] on ImageNet-1K. Note that we do not perform any extra training here. Our results show that using aggregated tokens consistently exceeds the performances of those without token aggregation across all metrics. This suggests that aggregating contextually related tokens can address inconsistencies and lead to performance gains.

Note that the final metric we use is an alternative: a patch-wise continuous similarity metric. We measure the cosine similarity between the [CLS] token and each patch, which is also a patch-wise metric but continuous<sup>1</sup>. As observed in Table 1, the averaged similarities are computed to 0.56 vs. 0.53 for each case. This new metric, directly linked to the [CLS] token, suggests a more direct relationship between improved accuracy and reduced spatial inconsistency. The trend aligns with the other discrete metric, depicting patch-wise classification of 30.8% and 26.5% with and without token aggregation, respectively. The quantitative assessments, using both continuous and discontinuous metrics, demonstrate that token representations exhibit spatial inconsistency. Taking this further, we believe more effectively addressing inconsistency would yield a greater impact.

### 3.3 Spatial Inconsistency in Representation Learning

We now study the impact of token aggregation on representation learning. This analysis aims to highlight the spatial inconsistency in self-distillation signal could

<sup>1</sup> We further involve a continuous metric to assess spatial inconsistency, as it tracks network responses continuously compared with discrete classification metrics.

**Table 2: Self-distillation signals should be aware of context.** We evaluate the ImageNet-1K linear probing accuracy of self-distillation supervisions (Fig 2). The baseline demonstrates efficacy as token-wise supervision directly benefits the tokens; only more refined signals could surpass it (lower rows). Upper rows showcase simpler targets, utilizing fundamental methods, only achieving efficiency without accuracy gains.

Distillation signals	Linear prob (%)	Speed↓ (ms/img)
(1) Token-wise (baseline)	70.9	0.629
(2) Downsampling	68.8 (-2.1)	0.647
(3) Layer-wise Bipartite Matching [6]	70.2 (-0.7)	0.633
(4) Superpixel clustering [2]	72.6 (+1.7)	0.740
(5) Token morphing via Bipartite Matching	72.2 (+1.3)	0.653

potentially diminish the quality of representations. Our comparison ranges distillations with the signals of 1) token-wise, 2) downsampling, 3) layer-wise bipartite matching during encoding, 4) superpixel, and 5) token morphing via bipartite matching. Note that token morphing will be introduced in §4.1, but we show its effectiveness in advance. We pre-train ViT-B/16 for 50 epochs and perform linear probing for 50 epochs on ImageNet-1K for each configuration.

First, Table 2 exhibits distillation with token aggregation methods such as token morphing via bipartite matching, and superpixel clustering outperforms that of the token-wise distillation approach. Once again, this reveals that token representations indeed exhibit spatial inconsistency, as we claimed. Furthermore, token aggregation methods for contextually related tokens could manage this inconsistency. Since the downsampling approach aggregates tokens without context awareness, and the layer-wise bipartite matching approach risks harming intermediate representations during encoding, both approaches exhibit diminished returns. The findings highlight the significance of employing context-aware token aggregations that preserve token count while addressing spatial inconsistency.

Despite superpixel clustering’s promising results, our pilot study finds that our method learning with 1) superpixel clustering and 2) context-aware bipartite matching yields accuracies of 87.1% and 87.9%, respectively, over 100 epochs trained on ImageNet-100. Therefore, we do not employ a superpixel-based clustering for our method, which is inefficient as well.

## 4 Method - Dynamic Token Morphing

We observed that 1) pre-trained models often produce noisy, spatial inconsistency token-level targets for learning, closely linked with performance degradation; 2) token aggregation methods could handle spatial inconsistency but are insufficient as a supervisory signal; 3) a well-designed method is needed to consider context and reduce noise more effectively. Motivated by the observations, we introduce an advanced token aggregation method *Dynamic Token Morphing* (DTM) for masked image modeling and self-supervised pre-training. In DTM, we contextually aggregate tokens to derive random numbers of morphed tokens aiming to encapsulate diversified semantic information. The core idea of DTM is

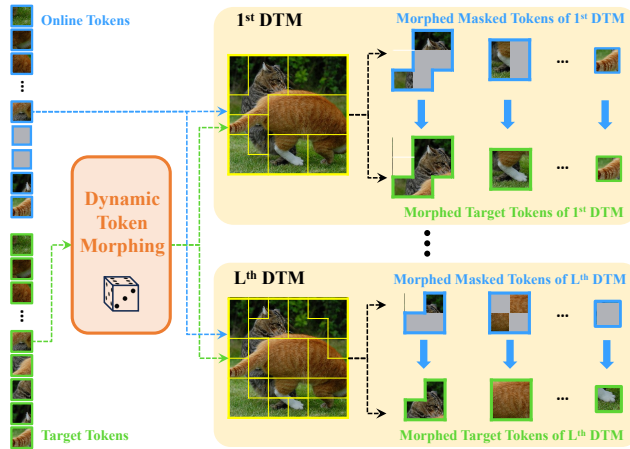


**Fig. 3: Token Morphing offers diverse and highly contextualized signals.** Dynamic Token Morphing (DTM) aligns the representations of tokens, based on a dynamic aggregation of contextually related ones. Note that DTM processes a multitude of morphed tokens to create more diverse and generalized targets. Blue and Green tokens denote the representations of the image patches processed by online and target models, respectively. Gray tokens represent masked tokens.

illustrated in Fig. 3, where the DTM module is straightforwardly added to the baseline MIM scheme. DTM is demonstrated for learning conventional token-level MIMs by aligning morphed tokens from online and target encoders.

#### 4.1 Preliminary

**Token encoding.** Given an image  $x$ , we patchify the image into  $N$  patches  $\{x_i\}_{i=1}^N$ . We select positions  $\mathcal{M} \subset \{1, 2, \dots, N\}$  of masked patches in a block-wise manner with a masking ratio  $r \in (0, 1)$  so that  $|\mathcal{M}| = \lfloor rN \rfloor$ . We mask the image patches by replacing the image patches of the position in  $\mathcal{M}$  to a learnable mask token  $e_{[mask]}$ . To this end, the input of the encoders becomes  $\{x_i^{\mathcal{M}}\}_{i=1}^N$  where  $x_i^{\mathcal{M}} = e_{[mask]}$  for  $i \in \mathcal{M}$  and  $x_i^{\mathcal{M}} = x_i$  for  $i \notin \mathcal{M}$ . The masked patches  $\{x_i^{\mathcal{M}}\}_{i=1}^N$  are concatenated with a learnable CLS token  $e_{[CLS]}$  and fed into the online encoder  $f_\theta$  with a subsequent linear head  $h_\theta$  and the target encoder  $f_\xi$ , and become encoded online tokens  $\{\mathbf{u}_i\}_{i=1}^N$  and  $\{\mathbf{v}_i\}_{i=1}^N$  where  $\mathbf{u}_i = h_\theta(f_\theta(x_i^{\mathcal{M}}))$  and  $\mathbf{v}_i = f_\xi(x_i^{\mathcal{M}})$ , respectively.

**Token morphing.** Differ to token aggregation methods, which prioritize efficiency via token reduction, token morphing specifically targets the spatial inconsistency in token representations by taking context into account. It connects contextually relevant tokens to smooth them without reducing the number of tokens (*i.e.*, maintaining the token count). We define the process with the token morphing function  $\phi_R(\cdot)$  based on the morphing schedule  $R$ , a sequence of token numbers to morph. Here,  $\phi_R$  is a general notation for a function



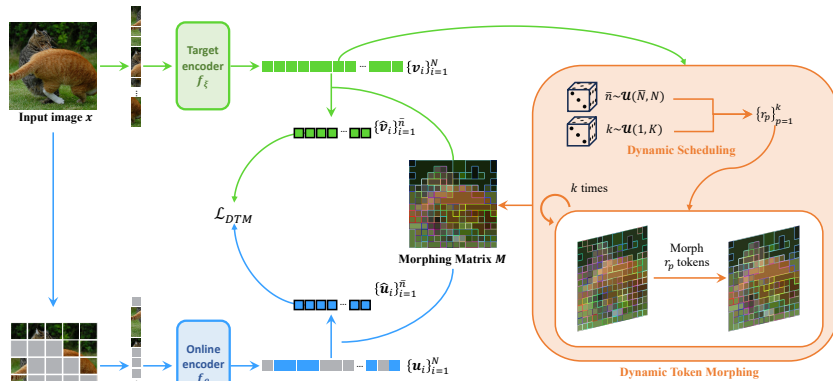


**Fig. 4: Overview of Masked Image Modeling via Dynamic Token Morphing (DTM).** For a token morphing schedule of DTM, we aggregate the dynamic range of tokens using morphing matrix  $M$  derived from target tokens  $\{\mathbf{v}_i\}_{i=1}^N$ . Specifically, we randomly sample a number of remaining tokens  $\bar{n}$  and an iteration number  $k$  to dynamically schedule token morphing (i.e.,  $\{r_p\}_{p=1}^k$ ), forming  $\bar{n}$  morphed tokens  $\{\hat{\mathbf{u}}_i\}_{i=1}^{\bar{n}}$  and  $\{\hat{\mathbf{v}}_i\}_{i=1}^{\bar{n}}$ . Then, we align representations of the corresponding online and target morphed tokens.

$\phi_R : \mathbb{R}^{N \times d} \rightarrow \{0, 1\}^{\bar{n} \times N}$  that calculates similarity using a matching algorithm (e.g., bipartite matching or K-Means clustering) and returns a token morphing matrix  $M = [M_{ij}] \in \{0, 1\}^{\bar{n} \times N}$ , where  $\bar{n}$  means the number of token groups after morphing. Eventually, we can morph tokens following Eq. 3.

## 4.2 Overall Pipeline of Dynamic Token Morphing

We present a more advanced token morphing method, Dynamic Token Morphing (DTM), here. DTM’s dynamic nature stems from its simultaneous exploration of multiple and diverse token morphing cases. This design is based on the insight that morphing numerous tokens enhances the denoising effect while morphing fewer tokens retains detailed token representations. Essentially, the diversity in the process would yield significant benefits. Since morphing a fixed number of tokens may benefit only one side, DTM balances these advantages by morphing a diverse range of tokens. Furthermore, to achieve diversified morphed tokens, we divide the morphing process into multiple processes to create multiple morphed tokens. To this end, DTM encompasses three key components: 1) *dynamic scheduler* for token counts, 2) *token morphing via scheduler*, and 3) *aligning morphed tokens*. The overall framework of DTM is described in Fig. 4.

**Dynamic scheduler.** DTM generates multiple morphed tokens to ensure diversity and an extensive range of token variations. To this end, we first sample the final number of morphed tokens  $\bar{n} \sim \mathcal{U}(\bar{N}, N)$  to remain after token morphing and the iteration number  $k \sim \mathcal{U}(1, K)$  from uniform distributions, where  $\bar{N}$



represents the minimum number of morphed tokens and  $K$  denotes the maximum number of iteration for sampling. Then, we define a token count scheduler  $R = \{r_p\}_{p=1}^k$ , a sequence of token numbers  $r_p$  that determines the number of tokens to morph for each iteration dynamically. Rather than sampling a sequence of random numbers  $r_p$  that satisfies  $\sum_{p=1}^k r_p = N - \bar{n}$ , we simply divide  $N - \bar{n}$  by  $k$  for constant counts:

$$r_p = \begin{cases} \lfloor (N - \bar{n})/k \rfloor, & \text{if } p < k \\ N - \bar{n} - (k - 1)\lfloor (N - \bar{n})/k \rfloor, & \text{if } p = k. \end{cases} \quad (1)$$

**Token morphing via dynamic scheduler.** The token morphing function  $\phi_R$  is dynamically changed based on randomly sampled  $\bar{n}$  and  $k$ . While our DTM is universal to any token matching methods, we employ bipartite matching [24] to search for contextually similar tokens efficiently. Specifically, we split tokens into two groups, with each token in the first group matched to its closest cosine similarity counterpart in the second group.

Eventually, we obtain the token morphing matrix  $M$ , a contextual relation among tokens, from the target token representations  $\{\mathbf{v}_i\}_{i=1}^N$  as follows:

$$M = \phi_R(\{\mathbf{v}_i\}_{i=1}^N), \quad (2)$$

where  $M_{ij} = 1$  indicates that the  $j^{\text{th}}$  token  $\mathbf{v}_j$  will be aggregated to the  $i^{\text{th}}$  token  $\mathbf{v}_i$ . In addition, every token should be assigned to a specific cluster, even in cases where it forms a single token cluster, and each token should retain its exclusive association with a single cluster (i.e.,  $\sum_i \sum_j M_{ij} = N$  and  $\sum_i M_{ij} = 1$ ). For the repetition  $p=1, \dots, k$ ,  $r_p$  token pairs are successively matched.

Based on the token morphing matrix  $M$  obtained by  $\phi_R$ , the representations for online and target morphed tokens are derived by:

$$\begin{aligned} \hat{\mathbf{u}}_i &= \sum_j M_{ij} \mathbf{u}_j, \\ \hat{\mathbf{v}}_i &= \sum_j M_{ij} \mathbf{v}_j, \end{aligned} \quad (3)$$

where  $\{\hat{\mathbf{u}}_i\}_{i=1}^{\bar{n}}$  and  $\{\hat{\mathbf{v}}_i\}_{i=1}^{\bar{n}}$  denote for the representations of online and target morphed tokens, respectively. Note that the morphed tokens are representative tokens for each token group, with their representations being smoothed specific to their respective groups.

**Aligning morphed tokens.** We formulate the objective function by accumulating DTM losses, which aligns the representations of the corresponding online and target morphed tokens derived by DTM. The DTM loss with sampled  $\bar{N}$  and  $k$  is formulated as follows:

$$\mathcal{L}_{\text{DTM}}(\bar{n}, k) = \sum_{i=1}^{\bar{n}} w_i d(\hat{\mathbf{u}}_i, \hat{\mathbf{v}}_i), \quad (4)$$

where  $d(\cdot)$  is a distance function and  $w_i = \sum_j M_{ij}$  is a number of tokens aggregated for the  $i^{\text{th}}$  online and target morphed tokens. Here, we utilize  $w_i$  to consider all tokens aggregated for the morphed tokens. Note that our DTM loss can be extended to token-wise or image-level losses when  $\bar{n} = N$  or  $\bar{n} = 1$ , respectively. We adopt Cosine distance for the distance function in Eq. (4) for all the DTM losses. To further enhance the dynamism of our method, we concurrently apply multiple DTMs. Therefore, the final objective function is the summation of all DTM losses, which is defined as:

$$\min_{\theta} \sum_{l=1}^L \mathcal{L}_{\text{DTM}}(\bar{n}_l, k_l) \quad \text{where } \bar{n}_l \sim \mathcal{U}(\bar{N}_l, N) \text{ and } k_l \sim \mathcal{U}(1, K_l), \quad (5)$$

where  $L$  denotes the total number of simultaneously employed DTMs.

## 5 Experiment

**Pre-training setup.** We pre-train our framework and other SSL frameworks through DTM on ImageNet-1K. We train our framework with ViT-S/16, ViT-B/16, and ViT-L/16 for 300 epochs using AdamW with momentum (0.9, 0.98) and a batch size of 1024. We use a learning rate of  $1.5 \times 10^{-4}$  with cosine decay and warmup 10 epochs. We employ the CLIP base models [35] with its visual projector as a target model across all scales of ViT. Block-wise masking is used with a ratio of 0.4 following [5, 34]. Cosine distance is used as a distance metric for the objective according to an ablation study in Appendix. For the hyperparameters of DTM, we used 2 for  $L$ , 1 for  $\bar{N}_1$ , 147 for  $\bar{N}_2$ , and 14 for all  $K_l$ . We also pre-train various SSL frameworks through our DTM with the same fundamental setups. More detailed setups for pre-training are detailed in Appendix. All models are pre-trained using 8 V100-32GB GPUs.

**Fine-tuning setup.** We fine-tune our pre-trained models on ImageNet-1K [39] by default following the standard protocol [19, 34]. Pre-trained ViT-S, ViT-B, and ViT-L are fine-tuned for 300, 100, and 50 epochs, respectively. Optimization is performed with AdamW using a weight decay of 0.05. We use a layer-wise learning rate decay of 0.6 for ViT-S and ViT-B and 0.8 for ViT-L. Learning rate is set to  $5 \times 10^{-4}$  with a linear warmup for 10 epochs for ViT-S and ViT-B and 5 epochs for ViT-L. Additional fine-tuning details are listed in Appendix.

### 5.1 ImageNet-1K Classification

We compare the fine-tuning accuracy of our method with previous state-of-the-art self-supervised methods on ImageNet-1K [39] datasets. The comparisons include supervised learning and SSL methods with various supervision signals. When the target model is CLIP, we only compare models pre-trained with CLIP B/16 for 300 epochs for a fair comparison. Table 3 reports the fine-tuning accuracies of ViT-S/B/L backbones. We observe that our MIM pre-trained by DTM

**Table 3: ImageNet-1K performance comparisons.** All models were pre-trained and fine-tuned on ImageNet-1K. We evaluate the improvements in fine-tuning accuracies between the baseline and our method for ViT-S/16, ViT-B/16, and ViT-L/16 with a resolution of  $224 \times 224$ . All our models are pre-trained for 300 epochs, which reveals the cost-efficiency in training. We further show ADE20K semantic segmentation results for each model trained by the standard training protocol.

Method		Pre-training epochs			Supervision	ViT-S	ViT-B	ViT-L	Seg
		ViT-S	ViT-B	ViT-L					
<i>Supervised models</i>									
DeiT [42]	ICML 2021	-	-	-	Label	-	81.8	-	-
DeiT-III [43]	ECCV 2022	-	-	-	Label	-	83.8	84.2	49.3
Cosub [44]	CVPR 2023	-	-	-	Label	81.5	84.2	85.3	49.3
<i>Self-supervised models</i>									
MoCo v3 [12]	ICCV 2021	300	300	300	Pixel	81.7	83.2	84.1	47.3
BEiT [5]	ICLR 2021	300	800	800	DALL-E	81.7	83.2	85.2	47.1
DINO [7]	ICCV 2021	3200	1600	-	Feature	82.0	83.6	-	46.8
SplisMask [16]	arXiv 2021	300	300	-	Pixel+Feat	81.5	83.6	-	46.8
iBOT [56]	ICLR 2022	3200	1600	1000	Feature	82.3	84.0	84.8	50.0
MAE [19]	CVPR 2022	-	1600	1600	Pixel	-	83.7	85.6	48.1
SimMIM [52]	CVPR 2022	-	800	-	Pixel	-	83.8	-	-
MaskFeat [47]	CVPR 2022	-	1600	1600	Feature	-	84.0	85.7	-
ExtreMa [50]	arXiv 2022	-	300	-	Feature	-	83.7	-	47.9
CAE [11]	arXiv 2022	300	1600	1600	Pixel+Feat	82.0	83.9	86.3	50.2
CMAE [22]	arXiv 2022	-	1600	1600	Pixel+Feat	-	84.4	-	50.1
FD-CLIP [49]	arXiv 2022	-	300	-	CLIP B/16	-	84.9	-	52.8
BEiT v2 [34]	arXiv 2022	-	300	300	CLIP B/16	-	85.0	86.6	52.7
data2vec [4]	ICML 2022	-	800	1600	Feature	-	84.2	86.6	-
mc-BEiT [27]	ECCV 2022	-	800	800	VQGAN	-	84.1	85.6	47.0
MVP [48]	ECCV 2022	-	300	300	CLIP B/16	-	84.4	86.3	52.4
SdAE [13]	ECCV 2022	-	300	-	Pixel	-	84.1	-	48.6
MSN [3]	ECCV 2022	-	600	-	Feature	-	83.4	-	-
BootMAE [14]	ECCV 2022	-	800	800	Pixel+Feat	-	84.2	85.9	49.1
CAN [31]	arXiv 2022	-	1600	800	Pixel	-	83.6	84.7	-
SemMAE [26]	NIPS 2022	-	800	-	Pixel	-	83.3	-	46.3
ConMIM [54]	ICLR 2023	300	800	1600	Dictionary	79.8	83.7	85.5	46.0
RC-MAE [54]	ICLR 2023	1600	1600	1600	Pixel	82.0	83.6	86.1	-
MixedAE [9]	CVPR 2023	-	1600	-	Pixel	-	83.9	-	49.8
SIM [41]	CVPR 2023	-	1600	-	Feature	-	83.8	-	-
HPM [46]	CVPR 2023	-	800	800	Pixel	-	84.2	85.8	48.5
MIRL [21]	NeurIPS 2023	-	300	300	Pixel	-	84.1	85.4	-
DeepMIM [38]	arXiv 2023	-	300	-	CLIP B/16	-	84.8	-	-
dBOT [29]	ICLR 2024	-	1600	1600	Feature	-	84.5	86.6	49.5
CrossMAE [17]	arXiv 2024	800	800	800	Pixel	79.3	83.7	85.4	-
DTM (ours)		-	300	300	CLIP B/16	<b>83.2</b>	<b>85.4</b>	<b>86.7</b>	<b>53.1</b>

achieves 83.2%, 85.4%, and 86.7% top-1 accuracies with ViT-S/16, ViT-B/16, and ViT-L/16, respectively, which outperforms state-of-the-art performances across the scales. Specifically, our method surpasses MVP [48], DeepMIM [38], and BEiT v2 [34] by 1.0%p, 0.6%p, and 0.4%p on ViT-B/16, respectively. Moreover, our method outperforms other methods that leverage diverse supervision, demonstrating our method’s superiority among self-supervised learning methods.

**Table 4: Applicability of our DTM on various SSL frameworks.** We compare the fine-tuning accuracies between models pre-trained by the vanilla SSL method and DTM. We adopt MAE [19] with CLIP teacher [35], BEiT v2 [34], and BYOL [18] to cover general SSL frameworks. We employ the ViT-B/16 architecture with a resolution of  $224 \times 224$ . All the models are pre-trained for 100 epochs.

Framework	Method	FT (%)
Feature MIM	MAE + CLIP	82.6
	MAE + CLIP + DTM	<b>83.2 (+0.6)</b>
(CLIP teacher)	BEiT v2	84.2
	BEiT v2 + DTM	<b>84.4 (+0.2)</b>
Image-level SSL	BYOL	81.7
	BYOL + DTM	<b>82.1 (+0.4)</b>

**Table 5: Scalibility check via varying scales of backbone architectures.** We highlight our method’s scalability compared with the baseline. We evaluate the improvements in fine-tuning accuracies between the baseline and our method for ViT-S/16, ViT-B/16, and ViT-L/16 with a resolution of  $224 \times 224$ . All the models are pre-trained for 300 epochs, which is efficient.

Method	ViT-S	ViT-B	ViT-L
MIM (Baseline)	82.7	84.3	86.4
DTM	<b>83.2</b>	<b>85.4</b>	<b>86.7</b>
Gain	<b>(+0.5)</b>	<b>(+1.1)</b>	<b>(+0.3)</b>

## 5.2 Effectiveness of Our Method

**Applicability on SSL frameworks.** We apply DTM on BEiT v2, MAE with the CLIP teacher [35], and BYOL [18] to verify its applicability to various SSL frameworks. As shown in Table 4, our DTM successfully improves the fine-tuning accuracy of MAE + CLIP, BEiT v2, and BYOL by 0.5%p, 0.2%p, and 0.4%p, which reveals its general applicability to various frameworks beyond our baseline.

**Scalability.** We further study the scalability of DTM. We compare the fine-tuning accuracies of our method to its baseline, which is pre-trained without DTM. We pre-train ViT-S/16, ViT-B/16, and ViT-L/16 with a resolution of  $224 \times 224$  for each method and evaluate the performance gains in fine-tuning accuracies. As shown in Table 5, DTM improved 0.4%p, 1.1%p, and 0.3%p for ViT-S/16, ViT-B/16, and ViT-L/16, respectively, verifying its general efficacy across the scales.

**Further Applicability on SLIP.** We apply DTM with the SLIP [32] to verify its applicability to various target models. We compare fine-tuning accuracies of the baseline and our method pre-trained by target patches from SLIP. Specifically, we generate target tokens using SLIP along with its projector. We pre-train ViT-B/16 with a resolution of  $224 \times 224$  for 300 epochs and fine-tune for 100 epochs on ImageNet-1K [39]. As shown in Table 6, our DTM successfully improves

**Table 6: Applicability of Dynamic Token Morphing (DTM) on SLIP.** We compare the fine-tuning accuracies between the baseline and our method pre-trained with SLIP [32], a more improved language-image pre-trained model. We observe that our method largely improves the fine-tuning performance, showcasing our method’s applicability beyond CLIP. We employ ViT-B/16 with a resolution of  $224 \times 224$ . All models are pre-trained for 300 epochs on ImageNet-1K.

Target models	Method	ViT-S	ViT-B	ViT-L
SLIP	Baseline	81.8	84.0	85.7
	DTM	82.1 (+0.3)	84.5 (+0.5)	86.1 (+0.4)

**Table 7: Efficiency of context-aware token aggregations.** We report fine-tuning accuracies and throughputs for each configuration, which are pre-trained with ViT-B/16. We compare DTM with Bipartite matching, DTM with K-Means clustering, and layer-wise K-Means clustering. For the layer-wise K-Means clustering, we use constant numbers of clusters and iterations. DTMs both outperform the baseline with large margins. Moreover, DTM with K-means clustering surpasses layer-wise K-means clustering, demonstrating the superiority of DTM.

Case	Throughput (image/s)	FT (%)
Baseline	<b>1458</b>	84.3
Layer-wise K-Means clustering	1265	85.1
DTM (K-Means clustering)	489	<b>85.4</b>
DTM (Bipartite matching)	1446	<b>85.4</b>

the fine-tuning accuracy of the baselines pre-trained with SLIP by 0.5%p, which reveals its general applicability beyond CLIP [35].

**Efficiency.** To verify the efficiency of our method, we compared Table 7 shows that bipartite matching is efficient and effective, significantly boosting the accuracy (+1.1%p) with only a 1% speed loss. While K-Means [30] also exhibits considerable improvements, it significantly degrades the training speed. Layer-wise K-Means shows accelerate the K-Means method by aggregating tokens within layers at the cost of degraded representations, leading to lower accuracy.

### 5.3 ADE20K Semantic Segmentation

We further evaluate semantic segmentation performance on ADE20K [55] to verify the transferability of our pre-trained model. We follow the training and evaluation protocol [19]; the models are fine-tuned for 160K iterations using UperNet [51] with a batch size of 16 and a resolution of  $512 \times 512$ . We initialize UperNet with our pre-trained ViT-B/16. Detailed hyperparameters for semantic segmentation fine-tuning can be found in Appendix. The first right column in Table 3 shows the mIoU performance comparison. Our method also outperforms the previous state-of-the-art results with a margin of 0.3%p, validating its superiority over other SSL methods. This result signifies that our method effectively enhances discriminability for dense prediction tasks.

**Table 8: Transfer learning results on iNaturalists.** We further present the end-to-end fine-tuning accuracies on the iNaturalist 2018, iNaturalist 2019, and mini iNaturalist 2021 datasets [45]. We report the best results along with the mean  $\pm$  std of the set of accuracies obtained from grid searches for each method. Our method consistently outperforms the competitors in terms of the best accuracies, further showcasing remarkable tuning robustness.

Method	iNat 2018	iNat 2019	iNat 2021-mini
Baseline	75.0 (74.6 $\pm$ 0.6)	81.1 (79.8 $\pm$ 1.0)	75.8 (75.2 $\pm$ 0.6)
DTM (Ours)	<b>78.5 (77.4<math>\pm</math>0.6)</b>	<b>81.9 (81.2<math>\pm</math>0.6)</b>	<b>78.4 (77.5<math>\pm</math>0.6)</b>

**Table 9: Transfer learning results on Fine-Grained Visual Classification (FGVC) datasets.** We present the end-to-end fine-tuning accuracies on multiple datasets, reporting the best results along with the mean  $\pm$  std of the accuracies from grid searches. Our Dynamic Token Morphing (DTM) outperforms the baseline at the best accuracies overall.

Method	Birds	CUB-200	CIFAR-10	CIFAR-100	Dogs	Average
Baseline	87.3 (86.5 $\pm$ 0.6)	87.1 (86.8 $\pm$ 0.6)	99.2 (99.1 $\pm$ 0.0)	92.0 (91.9 $\pm$ 0.3)	86.9 (86.8 $\pm$ 0.1)	90.5
DTM (Ours)	88.8 (88.2 $\pm$ 0.4)	88.8 (88.1 $\pm$ 0.4)	99.3 (99.2 $\pm$ 0.0)	92.3 (92.1 $\pm$ 0.2)	87.9 (87.8 $\pm$ 0.2)	<b>91.4 (+0.9)</b>

## 5.4 Transfer learning

**iNaturalist datasets.** We verify the improved transferability of our pre-trained model. We compare fine-tuning accuracies of the baseline and our proposed model on iNaturalist 2018, iNaturalist 2019, and mini iNaturalist 2021 [45], which are highly imbalanced with different numbers of images per class. All the models are ViT-B/16 with a resolution of  $224 \times 224$ . Following the protocol [25], we perform grid searches on learning rates and weight decay and report the maximum accuracy and the mean and standard deviation of the accuracies. Table 8 shows our DTM loss significantly improves the baseline with large margins, which reveals enhanced transferability.

**Fine-Grained Visual Classification (FGVC) datasets.** We further validate the transferability of our method. Following the evaluation protocol as above, we conduct comparisons on FGVC datasets. Specifically, we evaluate fine-tuning accuracies on Birds, CUB-200, CIFAR-10, CIFAR-100, and Dogs through grid searches with different learning rates and weight decays. As shown in Table 9, our method outperforms the baseline overall across the datasets, which shows superior transferability and tuning robustness.

## 5.5 Ablation study

We conduct ablation studies on loss functions, the range of token morphing steps, and target normalization. We also study the impacts of the number of morphing schedules. We pre-train ViT-B/16 with a resolution of  $224 \times 224$  for 100 epochs and fine-tune for 100 epochs on ImageNet-1K [39].

**Table 10: Ablation studies on a single DTM schedule.** We perform ablation studies on loss functions, ranges of token morphing steps, and target normalization. All the studies report fine-tuning accuracies for each configuration pre-trained using ViT-B/16. All models are pre-trained for 100 epochs. We mark the default settings for the study in gray .

Case	Fine-tuning (%)	Case	Fine-tuning (%)
$\ell_1$	84.5	$\mathcal{U}(1, 7)$	84.7
$\ell_2$	84.6	$\mathcal{U}(1, 14)$	<b>84.8</b>
Smoothed $\ell_1$	84.4	$\mathcal{U}(1, 28)$	84.7
Cosine distance (Cos)	<b>84.8</b>		

(a) Loss function
(b) Morphing steps

**Table 11: Ablation study on dynamic mechanism.** We investigate the efficacy of the dynamic mechanism in DTM, revealing its significant contribution to our method.

Method	$\mathcal{L}_{\text{Token Morphing}}$	Dynamic	FT (%)
Baseline	-	-	84.3
DTM	✓	-	84.0 (-0.3)
DTM	✓	✓	<b>85.4 (+1.1)</b>

**Loss function.** We compare various options for the loss function in our method. We compared  $\ell_1$ ,  $\ell_2$ , smoothed  $\ell_1$ , and cosine distance. As shown in Table 10a, the model pre-trained using cosine distance outperforms the models with other distance functions.

**Range of token morphing iterations.** We compare fine-tuning accuracies of the pre-trained models while varying the ranges that randomly samples the number of morphing iterations in Table 10b. While our DTM works for all the sampling ranges, K=14 works best.

## 5.6 Analysis

**Ablation study on the importance of dynamics.** Table 11 presents an ablation study on the effectiveness of the dynamic mechanism on DTM. We employ ViT-B/16 [15] with a resolution of  $224 \times 224$ . The models are pre-trained for 300 epochs and fine-tuned for 100 epochs on ImageNet-1K [39]. For token morphing without the dynamic mechanism, half of the total 196 tokens are aggregated for each image. As shown in Table 11, token morphing with dynamic mechanism significantly improves the baseline while performance degrades without the dynamic mechanism, demonstrating the importance of dynamic mechanism in DTM.

**Faster convergence of DTM.** We analyze the behaviors of models pre-trained by DTM and token-wise objectives in Fig. 5. All the approaches employ CLIP representations for the target. As shown in Fig. 5a, the fine-tuning accuracies of DTM surpass the accuracy of the token-wise supervision approaches. Fig. 5b



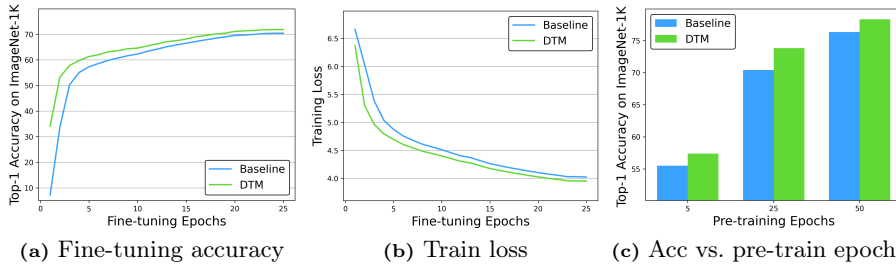


**Fig. 5: Visualizations with DTM.** We plot (a) top-1 accuracies and (b) training losses during fine-tuning on ImageNet-1K for models pre-trained by Dynamic Token Morphing (DTM) versus its baseline. (c) confirms the impact of pre-training epochs for DTM over the baseline. We train the ViT-B/16 architectures with a resolution of  $224 \times 224$ . In both (a) and (b), DTM consistently exhibits a substantial gap compared to the baseline during the entire fine-tuning phase, indicating that DTM offers stronger supervision that facilitates training. DTM consistently improves the baseline regardless of the pre-training epochs, as shown in (c).

shows that the model pre-trained by DTM exhibits a lower fine-tuning loss than the baseline model, verifying better convergence. Finally, Fig. 5c verifies the consistent effect of DTM across various pre-training epochs.

## 6 Conclusion

We have introduced a novel masked image modeling method based on token morphing to address the negative impacts of spatially inconsistent target representations during pre-training. We have first analyzed the existence and impacts of spatial inconsistency in target representations. Specifically, we qualitatively observed spatial inconsistency among tokens from pre-trained models despite proximity and contextual similarity. We then investigated the impacts on downstream tasks, including zero-shot/linear classification. We have further validated that context-aware token aggregation methods enhance the pre-training capability of the target tokens, while arbitrary aggregation, like downsampling, tends to disrupt them. Based on the observations, we have proposed Dynamic Token Morphing (DTM), which dynamically aggregates contextually associated tokens with a random number of matching tokens. Subsequently, our method aligns the representations of morphed tokens with the representations of their corresponding morphed targets. Our extensive experiments verified its general applicability, scalability, and superiority. We further validated its transferability, and subsequent analyses supported our method. Our study showcased that a token aggregation method could boost representation learning performance, with the potential for broader future applications and research directions.

**Limitation.** Despite the potential of our method, we have verified its applicability only up to ViT-L/16. Resource limitations prevented us from performing more experiments on larger-scale models such as ViT-G.

## References

1. Partitioning Around Medoids (Program PAM), chap. 2, pp. 68–125. John Wiley & Sons, Ltd (1990). <https://doi.org/https://doi.org/10.1002/9780470316801.ch2>, <https://onlinelibrary.wiley.com/doi/abs/10.1002/9780470316801.ch2> **3**
2. Achanta, R., Shaji, A., Smith, K., Lucchi, A., Fua, P., Süsstrunk, S.: Slic superpixels compared to state-of-the-art superpixel methods. *TPAMI* **34**(11), 2274–2282 (2012) **6, 21, 23**
3. Assran, M., Caron, M., Misra, I., Bojanowski, P., Bordes, F., Vincent, P., Joulin, A., Rabbat, M., Ballas, N.: Masked siamese networks for label-efficient learning. arXiv preprint arXiv:2204.07141 (2022) **11**
4. Baevski, A., Hsu, W.N., Xu, Q., Babu, A., Gu, J., Auli, M.: data2vec: A general framework for self-supervised learning in speech, vision and language. In: Chaudhuri, K., Jegelka, S., Song, L., Szepesvari, C., Niu, G., Sabato, S. (eds.) *ICML. Proceedings of Machine Learning Research*, vol. 162, pp. 1298–1312. PMLR (17–23 Jul 2022), <https://proceedings.mlr.press/v162/baevski22a.html> **1, 2, 11**
5. Bao, H., Dong, L., Piao, S., Wei, F.: Beit: Bert pre-training of image transformers. In: *ICLR* (2021) **1, 2, 10, 11**
6. Bolya, D., Fu, C.Y., Dai, X., Zhang, P., Feichtenhofer, C., Hoffman, J.: Token merging: Your vit but faster. arXiv preprint arXiv:2210.09461 (2022) **6**
7. Caron, M., Touvron, H., Misra, I., Jégou, H., Mairal, J., Bojanowski, P., Joulin, A.: Emerging properties in self-supervised vision transformers. In: *ICCV* (2021) **1, 11**
8. Chang, S., Wang, P., Lin, M., Wang, F., Zhang, D.J., Jin, R., Shou, M.Z.: Making vision transformers efficient from a token sparsification view. In: *Proceedings of the IEEE/CVF Conference on Computer Vision and Pattern Recognition*. pp. 6195–6205 (2023) **21, 23**
9. Chen, K., Liu, Z., Hong, L., Xu, H., Li, Z., Yeung, D.Y.: Mixed autoencoder for self-supervised visual representation learning. In: *CVPR*. pp. 22742–22751 (June 2023) **11**
10. Chen, T., Kornblith, S., Norouzi, M., Hinton, G.: A simple framework for contrastive learning of visual representations. arXiv preprint arXiv:2002.05709 (2020) **1**
11. Chen, X., Ding, M., Wang, X., Xin, Y., Mo, S., Wang, Y., Han, S., Luo, P., Zeng, G., Wang, J.: Context autoencoder for self-supervised representation learning. arXiv preprint arXiv:2202.03026 (2022) **11**
12. Chen, X., Xie, S., He, K.: An empirical study of training self-supervised vision transformers. arXiv preprint arXiv:2104.02057 (2021) **11**
13. Chen, Y., Liu, Y., Jiang, D., Zhang, X., Dai, W., Xiong, H., Tian, Q.: Sdae: Self-distilled masked autoencoder. In: *ECCV*. pp. 108–124. Springer (2022) **11**
14. Dong, X., Bao, J., Zhang, T., Chen, D., Zhang, W., Yuan, L., Chen, D., Wen, F., Yu, N.: Bootstrapped masked autoencoders for vision bert pretraining. arXiv preprint arXiv:2207.07116 (2022) **11**
15. Dosovitskiy, A., Beyer, L., Kolesnikov, A., Weissenborn, D., Zhai, X., Unterthiner, T., Dehghani, M., Minderer, M., Heigold, G., Gelly, S., Uszkoreit, J., Houlsby, N.: An image is worth 16x16 words: Transformers for image recognition at scale. In: *ICLR* (2021) **1, 15**
16. El-Nouby, A., Izacard, G., Touvron, H., Laptev, I., Jegou, H., Grave, E.: Are large-scale datasets necessary for self-supervised pre-training? arXiv preprint arXiv:2112.10740 (2021) **11**

17. Fu, L., Lian, L., Wang, R., Shi, B., Wang, X., Yala, A., Darrell, T., Efros, A.A., Goldberg, K.: Rethinking patch dependence for masked autoencoders. arXiv preprint arXiv:2401.14391 (2024) [11](#)
18. Grill, J.B., Strub, F., Altché, F., Tallec, C., Richemond, P., Buchatskaya, E., Doersch, C., Avila Pires, B., Guo, Z., Gheshlaghi Azar, M., Piot, B., koray Kavukcuoglu, Munos, R., Valko, M.: Bootstrap Your Own Latent - A New Approach to Self-Supervised Learning. In: Larochelle, H., Ranzato, M., Hadsell, R., Balcan, M.F., Lin, H. (eds.) NeurIPS. vol. 33, pp. 21271–21284. Curran Associates, Inc. (2020) [1](#), [12](#), [25](#)
19. He, K., Chen, X., Xie, S., Li, Y., Dollár, P., Girshick, R.: Masked autoencoders are scalable vision learners. In: CVPR. pp. 16000–16009 (June 2022) [1](#), [2](#), [10](#), [11](#), [12](#), [13](#), [24](#), [25](#)
20. He, K., Fan, H., Wu, Y., Xie, S., Girshick, R.: Momentum contrast for unsupervised visual representation learning. arXiv preprint arXiv:1911.05722 (2019) [1](#)
21. Huang, G., Fu, H., Bors, A.G.: Masked image residual learning for scaling deeper vision transformers. NeurIPS **36** (2024) [11](#)
22. Huang, Z., Jin, X., Lu, C., Hou, Q., Cheng, M.M., Fu, D., Shen, X., Feng, J.: Contrastive masked autoencoders are stronger vision learners. arXiv preprint arXiv:2207.13532 (2022) [11](#)
23. Jiang, J., Chen, Y., Meng, X., Wang, L., Li, K.: A novel density peaks clustering algorithm based on k nearest neighbors for improving assignment process. Physica A: Statistical Mechanics and its Applications **523**, 702–713 (2019). <https://doi.org/https://doi.org/10.1016/j.physa.2019.03.012>, <https://www.sciencedirect.com/science/article/pii/S0378437119302316> [3](#)
24. Karp, R.M., Vazirani, U.V., Vazirani, V.V.: An optimal algorithm for on-line bipartite matching. In: Proceedings of the twenty-second annual ACM symposium on Theory of computing. pp. 352–358 (1990) [3](#), [9](#)
25. Kornblith, S., Shlens, J., Le, Q.V.: Do better imagenet models transfer better? In: CVPR. pp. 2661–2671 (2019) [14](#)
26. Li, G., Zheng, H., Liu, D., Wang, C., Su, B., Zheng, C.: Semmae: Semantic-guided masking for learning masked autoencoders. arXiv preprint arXiv:2206.10207 (2022) [11](#)
27. Li, X., Ge, Y., Yi, K., Hu, Z., Shan, Y., Duan, L.Y.: mc-beit: Multi-choice discretization for image bert pre-training. In: ECCV (2022) [1](#), [11](#)
28. Liang, Y., GE, C., Tong, Z., Song, Y., Wang, J., Xie, P.: EVit: Expediting vision transformers via token reorganizations. In: ICLR (2022), [https://openreview.net/forum?id=BjyvvnXXVn\\_3](https://openreview.net/forum?id=BjyvvnXXVn_3)
29. xingbin liu, Zhou, J., Kong, T., Lin, X., Ji, R.: Exploring target representations for masked autoencoders. In: ICLR (2024), <https://openreview.net/forum?id=xmQMz90PF5> [11](#)
30. Lloyd, S.: Least squares quantization in pcm. IEEE Transactions on Information Theory **28**(2), 129–137 (1982). <https://doi.org/10.1109/TIT.1982.1056489> [3](#), [13](#)
31. Mishra, S., Robinson, J., Chang, H., Jacobs, D., Sarna, A., Maschinot, A., Krishnan, D.: A simple, efficient and scalable contrastive masked autoencoder for learning visual representations. arXiv preprint arXiv:2210.16870 (2022) [11](#)
32. Mu, N., Kirillov, A., Wagner, D., Xie, S.: Slip: Self-supervision meets language-image pre-training. arXiv preprint arXiv:2112.12750 (2021) [12](#), [13](#)
33. Pan, Z., Zhuang, B., He, H., Liu, J., Cai, J.: Less is more: Pay less attention in vision transformers. In: AAAI (2022) [3](#)

34. Peng, Z., Dong, L., Bao, H., Ye, Q., Wei, F.: BEiT v2: Masked image modeling with vector-quantized visual tokenizers (2022) [1](#), [3](#), [10](#), [11](#), [12](#), [24](#), [25](#)
35. Radford, A., Kim, J.W., Hallacy, C., Ramesh, A., Goh, G., Agarwal, S., Sastry, G., Askell, A., Mishkin, P., Clark, J., Krueger, G., Sutskever, I.: Learning transferable visual models from natural language supervision. In: ICML (2021) [3](#), [4](#), [5](#), [10](#), [12](#), [13](#), [21](#), [25](#)
36. Ramesh, A., Pavlov, M., Goh, G., Gray, S., Voss, C., Radford, A., Chen, M., Sutskever, I.: Zero-shot text-to-image generation. In: ICML. pp. 8821–8831. PMLR (2021) [2](#)
37. Rao, Y., Zhao, W., Liu, B., Lu, J., Zhou, J., Hsieh, C.J.: Dynamicvit: Efficient vision transformers with dynamic token sparsification. NeurIPS **34**, 13937–13949 (2021) [3](#)
38. Ren, S., Wei, F., Albanie, S., Zhang, Z., Hu, H.: Deepmim: Deep supervision for masked image modeling. arXiv preprint arXiv:2303.08817 (2023) [3](#), [11](#)
39. Russakovsky, O., Deng, J., Su, H., Krause, J., Satheesh, S., Ma, S., Huang, Z., Karpathy, A., Khosla, A., Bernstein, M., Berg, A.C., Fei-Fei, L.: Imagenet large scale visual recognition challenge. IJCV **115**(3), 211–252 (2015) [10](#), [12](#), [14](#), [15](#), [21](#), [23](#), [24](#)
40. Tang, Y., Han, K., Wang, Y., Xu, C., Guo, J., Xu, C., Tao, D.: Patch slimming for efficient vision transformers. In: CVPR. pp. 12165–12174 (2022) [3](#)
41. Tao, C., Zhu, X., Su, W., Huang, G., Li, B., Zhou, J., Qiao, Y., Wang, X., Dai, J.: Siamese image modeling for self-supervised vision representation learning. In: CVPR. pp. 2132–2141 (2023) [11](#)
42. Touvron, H., Cord, M., Douze, M., Massa, F., Sablayrolles, A., Jégou, H.: Training data-efficient image transformers & distillation through attention. In: ICML. vol. 139, pp. 10347–10357 (July 2021) [11](#)
43. Touvron, H., Cord, M., Jégou, H.: Deit iii: Revenge of the vit. In: ECCV. pp. 516–533. Springer (2022) [11](#)
44. Touvron, H., Cord, M., Oquab, M., Bojanowski, P., Verbeek, J., Jégou, H.: Co-training 2l submodels for visual recognition. In: CVPR. pp. 11701–11710 (2023) [11](#)
45. Van Horn, G., Mac Aodha, O., Song, Y., Cui, Y., Sun, C., Shepard, A., Adam, H., Perona, P., Belongie, S.: The inaturalist species classification and detection dataset. In: CVPR. pp. 8769–8778 (2018) [14](#), [25](#)
46. Wang, H., Song, K., Fan, J., Wang, Y., Xie, J., Zhang, Z.: Hard patches mining for masked image modeling. In: CVPR (2023) [11](#)
47. Wei, C., Fan, H., Xie, S., Wu, C.Y., Yuille, A., Feichtenhofer, C.: Masked feature prediction for self-supervised visual pre-training. In: CVPR (2022) [11](#)
48. Wei, L., Xie, L., Zhou, W., Li, H., Tian, Q.: Mvp: Multimodality-guided visual pre-training. In: ECCV. pp. 337–353. Springer (2022) [3](#), [11](#)
49. Wei, Y., Hu, H., Xie, Z., Zhang, Z., Cao, Y., Bao, J., Chen, D., Guo, B.: Contrastive learning rivals masked image modeling in fine-tuning via feature distillation. arXiv preprint arXiv:2205.14141 (2022) [1](#), [3](#), [11](#)
50. Wu, Z., Lai, Z., Sun, X., Lin, S.: Extreme masking for learning instance and distributed visual representations. arXiv preprint arXiv:2206.04667 (2022) [11](#)
51. Xiao, T., Liu, Y., Zhou, B., Jiang, Y., Sun, J.: Unified perceptual parsing for scene understanding. In: ECCV. Springer (2018) [13](#)
52. Xie, Z., Zhang, Z., Cao, Y., Lin, Y., Bao, J., Yao, Z., Dai, Q., Hu, H.: Simmim: A simple framework for masked image modeling. In: ICCV (2022) [1](#), [2](#), [11](#)

53. Xu, Y., Zhang, Z., Zhang, M., Sheng, K., Li, K., Dong, W., Zhang, L., Xu, C., Sun, X.: Evo-vit: Slow-fast token evolution for dynamic vision transformer. In: AAAI. vol. 36, pp. 2964–2972 (2022) [3](#)
54. Yi, K., Ge, Y., Li, X., Yang, S., Li, D., Wu, J., Shan, Y., Qie, X.: Masked image modeling with denoising contrast. ICLR (2023) [11](#)
55. Zhou, B., Zhao, H., Puig, X., Fidler, S., Barriuso, A., Torralba, A.: Scene parsing through ade20k dataset. In: CVPR (July 2017) [13](#), [21](#), [25](#)
56. Zhou, J., Wei, C., Wang, H., Shen, W., Xie, C., Yuille, A., Kong, T.: ibot: Image bert pre-training with online tokenizer. In: ICLR (2022) [1](#), [2](#), [11](#)

## Appendix

This appendix includes additional experimental analyses of our proposed method. First, we present additional examples of spatial inconsistency among patches from pre-trained models in §A. Then, we validate the applicability of superpixel algorithms [2] into DTM in §B. We also conduct ablation studies on number of morphing schedules and effects of randomness in the number of morphing tokens, randomness in gradual token morphing, and target normalization in §C. Finally, §D provides implementation details for both pre-training and fine-tuning on ImageNet-1K [39], as well as fine-tuning on ADE20K [55].

### A More Examples on Spatial Inconsistency

We further investigate the spatial inconsistency of patch representations generated by a pre-trained model across various samples. We visualize token morphing results and correct maps of the patch-wise prediction results with and without token morphing using CLIP [35]. Specifically, the correct maps provide information about both correct and incorrect predictions. Patches with correct predictions are highlighted in yellow, while incorrectly predicted patches exhibit results with monotone colors. As shown in Fig. A, patch representations without token morphing reveal spatially inconsistent patch-wise predictions compared to the prediction results with token morphing, which reveals the spatially inconsistent representations among patches. In addition, predictions with token morphing exhibit significantly more correctly predicted patches than predictions without token morphing.

### B Compatibility with Superpixel Algorithms

We perform additional experiments to use the concept of superpixels [2,8] in ours, both directly to tokens (layer-wise superpixel) and can be combined with DTM. The layer-wise superpixel method uses constant numbers of superpixels and iterations. Table A shows superpixel-based methods enjoy notable gains but do not exceed the bipartite matching one. While the layer-wise superpixel method also utilizes superpixels, the layer-wise token aggregation across the encoder layers bipartite matching approach risks harming intermediate representations during encoding

#### B.1 Ablation Study on the Number of Schedules

Our method can further enhance the diversity of target morphed tokens by employing multiple schedules within a single iteration. Thus, we study the effects of learning diverse morphed tokens derived from multiple morphing schedules simultaneously. We compare the fine-tuning accuracy of models pre-trained by our DTM, varying the number of schedules. We pre-train ViT-B/16 with a resolution



**Fig. A: Visualization of spatial inconsistency using CLIP.** We present patch-wise prediction results of a sample for zero-shot image classification to visualize the spatial inconsistent predictions among patches. For the given input images in (a), (b), and (c), visualize the predicted classes for each patch in the bounding boxes through patch-wise zero-shot classification with and without token morphing, respectively. Precisely, we depict the differences between the predicted classes and the ground-truth class by varying the lightness of red colors. We observe that the prediction results of the morphed tokens are more likely to align with the input patches, leading to a reduction in the spatial inconsistency incurred by patch-wise predictions.



**Table A: Applicability of DTM on the superpixel algorithm.** All the studies report fine-tuning accuracies for each configuration pre-trained using ViT-B/16. All models are pre-trained for 100 epochs on ImageNet-100. Here, the Layer-wise superpixel method denotes a token reduction approach that generates superpixel tokens across the layers. While the superpixel algorithm is applicable to DTM, Bipartite matching exhibits the best performance, demonstrating the superiority of our design choice. We mark the default settings for the study in gray .

Method	Fine-tuning (%)
Baseline	79.5
Layer-wise superpixel [2]	86.7
DTM (Superpixel clustering) [8]	87.1
DTM (Bipartite matching)	<b>87.9</b>

**Table B: Ablation study on the number of DTM schedules.** We study the effect of exploring diverse morphed tokens through multiple scheduling. We report fine-tuning accuracies for each configuration, which are pre-trained with ViT-B/16. All the backbones are pre-trained for 100 epochs on ImageNet-1K [39]. Simultaneous exploration using multiple morphing schedules further enhances the performance. We mark the default settings for the study in gray .

Method	Case	IN-1K Fine-tuning (%)	IN-100 Fine-tuning (%)
Baseline		83.5	79.5
	1	84.8	87.6
DTM	<b>2</b>	<b>84.9</b>	<b>87.9</b>
	3	84.8	87.8
	4	84.8	87.8

of  $224 \times 224$  for 100 epochs and fine-tune for 100 epochs on ImageNet-1K [39] and ImageNet-100 [39]. Table B reveals that exploring diverse target morphed tokens improves the representation capability of pre-trained models, leading to increased fine-tuning accuracies of at least 0.1%p and 0.2%p on ImageNet-1K and ImageNet-100 compared to the model pre-trained by the single DTM approach, respectively. However, the goal of experiencing diverse morphed tokens at once appears to be attained with double scheduling, resulting in no additional gains in performance through further exploration. Given that utilizing two schedules yields the best and is most efficient among all other multiple scheduling options, we adopt the double morphing scheduling approach.

## C Additional ablation studies

### C.1 Ablation Study on Randomness of DTM.

**Randomness in the number of morphing tokens.** Our DTM randomizes the number of morphing tokens since fixing the number of morphing tokens does not adequately generate diverse morphed tokens. To verify the effectiveness of

**Table C: Ablation study on various configurations.** We investigate the effectiveness of our design choices for DTM: morphing a random number of tokens, gradual morphing by multiple morphing steps, and target normalization. We report fine-tuning accuracies for each configuration. We adopt ViT-B/16 with a resolution of  $224 \times 224$ . All the models are pre-trained for 100 epochs on ImageNet-100 [39]. While other configurations improve the baseline well, our design yields the best accuracy. We mark the default settings for the study in gray .

Method	Configurations	Fine-tuning (%)
Baseline		79.5
	Fixed number of morphing tokens	87.4
	Single step morphing	87.7
DTM (ours)	+ Target normalization [19]	87.7
	Default	<b>87.9</b>

the randomness, we compare the fine-tuning accuracies of models pre-trained using DTM with random and fixed numbers of morphing tokens. We pre-train and fine-tune the models for 100 epochs on ImageNet-100 [39]. As reported in the 2nd and 5th rows of Table C, exploring diverse morphed tokens improves the fine-tuning accuracy by 0.5%p. This result demonstrates the impact of varying numbers of morphing tokens.

**Randomness in gradual token morphing.** As morphed tokens can vary by the number of morphing iterations, we apply randomness in token morphing iterations. We compare fine-tuning accuracies of the pre-trained models with random and fixed iteration numbers for morphing to validate the effect of randomness. As shown in the 3rd and 5th rows of Table C, randomly selecting the iteration number for morphing enhances the performance, confirming its effectiveness.

## C.2 Ablation Study on target normalization.

Target normalization is proven to have a significant impact on MAE [19]. Thus, we verify the impact of target normalization on our DTM. We employ ViT-B/16 with a resolution of  $224 \times 224$  for comparison. As shown in the 4th and 5th rows of Table C, target normalization does not yield a positive effect on our DTM, resulting in a decrease in fine-tuning accuracy from 87.9% to 87.7%.

## D Implementation details

**Pre-training on ImageNet-1K.** The pre-training recipe for DTM mainly follows the recipe of BEiT v2 [34]. Table D reports the implementation details for pre-training. We adopt the hyperparameters for ViT-B/16 and ViT-L/16 pre-training from BEiT v2. Specifically, we use layer scales of 0.1 and  $1 \times 10^{-5}$  for ViT-B/16 and ViT-L/16, respectively. We employ both relative positional

embeddings and shared relative positional embeddings. The maximum gradient value is constrained to 3.0. We apply color jittering followed by random resizing and cropping for data augmentation. The hyperparameters for ViT-S/16 replicate the settings of ViT-B/16.

**Fine-tuning on ImageNet-1K.** The fine-tuning recipe for DTM mainly follows the standard supervised learning recipe for ViT. Specifically, we adopt commonly used values for RandAugment, Mixup, Cutmix, and Label Smoothing. On the other hand, we employ relative positional embeddings. Stochastic depth is applied with values of 0.1, 0.1, and 0.2 for ViT-S/16, ViT-B/16, and ViT-L/16, respectively. The overall recipe is detailed in Table E.

**Fine-tuning on ADE20K.** Table F summarizes the fine-tuning recipe of ViT/16 for the semantic segmentation task on ADE20K [55]. We employ AdamW with momentum (0.9, 0.999) and warm-up for 1500 iterations. The learning rate is linearly scheduled with a value of  $5 \times 10^{-5}$ . We apply layer-wise learning rate decay of 0.75, stochastic depth of 0.1, and weight decay of 0.05. The model is fine-tuned using 8 V100-32GB GPUs.

**Transfer learning.** We follow the fine-tuning recipes for DTM to conduct transfer learning to iNaturalist datasets, including iNaturalist 2018, iNaturalist 2019, and mini iNaturalist 2021 [45] and FGVC datasets, including Birds, CUB-200, CIFAR-10, CIFAR-100, and Dogs. However, we additionally perform grid searches of learning rates and weight decay. Specifically, we fine-tune the models with learning rates of  $2.5 \times 10^{-5}$ ,  $5 \times 10^{-5}$ , and  $1 \times 10^{-4}$  and weight decays of 0.05 and 0.1.

**Applicability on various SSL frameworks.** When pre-training and fine-tuning models with MAE [19], BEiT v2 [34], and BYOL [18], we follow their vanilla training recipes. We pre-train and fine-tune ViT-B/16 for 100 epochs. However, we use CLIP [35] target features instead of patchified images to pre-train MAE.

**Table D:** Hyperparameters for pretraining on ImageNet-1K.

Hyperparameters	ViT-S/16	ViT-B/16	ViT-L/16
Layers	12	12	24
Hidden size	384	768	1024
FFN inner hidden size	1536	3072	4096
Attention heads	6	12	16
Layer scale	0.1	0.1	1e-5
Patch size		16 × 16	
Relative positional embeddings		✓	
Shared relative positional embeddings		✓	
Training epochs		300	
Batch size		1024	
Adam $\beta$		(0.9, 0.98)	
Base learning rate		1.5e-4	
Learning rate schedule		Cosine	
Warmup epochs		10	
Gradient clipping		3.0	
Dropout		✗	
Drop path		0	
Weight decay		0.05	
Data Augment		RandomResizeAndCrop	
Input resolution		224 × 224	
Color jitter		0.4	

**Table E:** Hyperparameters for fine-tuning on ImageNet-1K.

Hyperparameters	ViT-S/16	ViT-B/16	ViT-L/16
Fine-tuning epochs	300	100	50
Warmup epochs	10	10	5
Layer-wise learning rate decay	0.6	0.6	0.8
Batch size		1024	
Adam $\epsilon$		1e-8	
Adam $\beta$		(0.9, 0.999)	
Base learning rate		5e-4	
Learning rate schedule		Cosine	
Repeated Aug		✗	
Weight decay		0.05	
Label smoothing $\epsilon$		0.1	
Stoch. depth	0.1	0.1	0.2
Dropout		✗	
Gradient clipping		✗	
Erasing prob.		0.25	
Input resolution		224 × 224	
Rand Augment		9/0.5	
Mixup prob.		0.8	
Cutmix prob.		1.0	
Relative positional embeddings		✓	
Shared relative positional embeddings		✗	

**Table F:** Hyperparameters for fine-tuning on ADE20K.

<b>Hyperparameters</b>	<b>ViT-B/16</b>
Input resolution	$512 \times 512$
Peak learning rate	5e-5
Fine-tuning steps	160K
Batch size	16
Adam $\epsilon$	1e-8
Adam $\beta$	(0.9, 0.999)
Layer-wise learning rate decay	0.75
Minimal learning rate	0
Learning rate schedule	Linear
Warmup steps	1500
Dropout	$\times$
Stoch. depth	0.1
Weight decay	0.05
Relative positional embeddings	$\checkmark$
Shared relative positional embeddings	$\times$